EES Solar

PAPER

Published on 07 August 2026
Licensed under CC-BY-NC 4.0

Check for updates

Cite this: *EES Sol.*, 2026, **2**, 1236

Co-spacer engineering enables targeted phase selection in quasi-2D halide perovskites *via* automated multimodal experimentation

Elham Foadian,†[a] Yifan Yu,†[b] Sheryl L. Sanchez,[a] Benjamin J. Lawrie,[cd] Hochan Song,[a] Jordan Marshall,[a] Byeong Jun Kim,[b] Subeom Shin,[e] Jared D. Fletcher,[f] Mercouri G. Kanatzidis,[f] Hyosung Choi,*[b] Jonghee Yang,*[e] Yongtao Liu*[c] and Mahshid Ahmadi*[a]

Targeted phase control in quasi-2D halide perovskites (HPs) is critical for engineering their optoelectronic functionality, yet deterministic phase control remains difficult because spacer chemistry, precursor assembly and crystallization kinetics evolve in a strongly coupled manner during film formation. Here, we introduce a multimodal, closed-loop autonomous experimentation workflow that couples automated *in situ* photoluminescence (PL) monitoring with high-throughput combinatorial synthesis, Gaussian process–Bayesian optimization (GP–BO), and X-ray diffraction (XRD) similarity scoring to achieve targeted 3D-like phase selection in quasi-2D HPs. Using a ternary compositional space consisting of $FAPbI_3$ and two structurally distinc Dion–Jacobson (DJ) co-spacers, 1,4-butanediammonium (BDA) and 3-(aminomethyl) piperidinium (3AMP), automated *in situ* PL reveals distinct phase evolution and crystallization pathways. BDA-based compositions rapidly evolve toward a 3D-like emissive phase, whereas 3AMP-based compositions show delayed phase evolution and broader emission associated with intermediate quasi-2D domains. By systematically varying the co-spacer ratio, the phase evolution trajectory can be tuned to favor convergence toward the target 3D-like phase. Guided by these observations, the GP–BO workflow screened 480 compositions across five autonomous iterations to identify co-spacer ratios, with XRD similarity scoring providing structural validation of optically identified candidates. Two distinct compositional regimes, BDA-rich and 3AMP-rich, were identified in which the balance between rapid framework formation and gradual structural reorganization converges on the target 3D-like phase. Spatial phase homogeneity in both regimes was confirmed by hyperspectral cathodoluminescence mapping. This work establishes co-spacer-mediated kinetic modulation as a design strategy for deterministic phase selection in quasi-2D HPs, and demonstrates a cross-facility self driving lab (SDL) framework for autonomous phase-targeted materials discovery.

Received 7th June 2026
Accepted 3rd August 2026

DOI: 10.1039/d6el00105j

rsc.li/EESSolar

Broader context

Quasi-2D halide perovskites are promising materials for next-generation photovoltaic technologies because they offer improved environmental stability, compositional tunability, and defect tolerance compared with conventional 3D perovskites. However, their broader implementation in solar energy applications remains limited by the difficulty of deterministic phase selection. In these systems, spacer chemistry, precursor assembly, and nonequilibrium crystallization dynamics are strongly coupled, leading to competing phase formation within narrow processing windows and making optical performance difficult to directly connect with structural phase identity. Here, we address this bottleneck by developing a multimodal autonomous experimentation workflow for targeted phase selection in Dion–Jacobson quasi-2D halide perovskites. By combining automated *in situ* photoluminescence monitoring, high-throughput synthesis and optical spectroscopy, Gaussian process–Bayesian optimization, and XRD, we identify co-spacer compositions that converge toward structurally verified 3D-like phases through distinct crystallization pathways. This work establishes co-spacer-mediated kinetic modulation as a design principle for deterministic phase selection in quasi-2D perovskites, while demonstrating a multimodal self-driving laboratory workflow that links real-time optical feedback with structural validation. More broadly, it provides a transferable strategy for connecting film-formation dynamics to phase identity in photovoltaic perovskites and related functional materials.

[a]*Institute for Advanced Materials and Manufacturing, Department of Materials Science and Engineering, University of Tennessee, Knoxville, TN 37996, USA. E-mail: mahmadi3@utk.edu*

[b]*Department of Chemistry, Research Institute for Natural Science, Research Institute for Convergence of Basic Science, Hanyang University, Seoul 04763, Republic of Korea. E-mail: hschoi202@hanyang.ac.kr*

[c]*Center for Nanophase Materials Sciences, Oak Ridge National Laboratory, Oak Ridge, TN 37831, USA. E-mail: liuy3@ornl.gov*

[d]*Materials Science and Technology Division, Oak Ridge National Laboratory, Oak Ridge, TN 37831, USA*

[e]*Department of Chemistry, Yonsei University, Seoul 03722, Republic of Korea. E-mail: jhyang@yonsei.ac.kr*

[f]*Department of Chemistry, Northwestern University, Evanston, IL 60208, USA*

† These authors contributed equally.

© 2026 The Author(s). Published by the Royal Society of Chemistry

Introduction

Formamidinium lead iodide ($FAPbI_3$) is a widely studied halide perovskite (HP) semiconductor with an ideal bandgap (~1.47 eV) for high-efficiency single-junction photovoltaics.[1–5] However, the practical realization of $FAPbI_3$ is hindered by the intrinsic instability of its photoactive black perovskite phase (*i.e.*, α-$FAPbI_3$), which readily transforms into the non-perovskite δ-phase under ambient conditions.[6–8] The formation and retention of the α-phase are strongly governed by synthesis variables, including precursor composition, solvent environment, annealing temperature, and processing time, all of which are highly interdependent.[9–11] Consequently, identifying a synthetic protocol that reproducibly stabilizes the α-$FAPbI_3$ phase across this vast parameter space remains challenging.

A promising strategy is to incorporate organic spacer cations into the 3D framework, forming quasi-2D structures that are thermodynamically more stable, processable at lower temperatures and capable of preserving near optimal bandgaps.[12–17] In quasi-2D systems, the target is a 3D-like phase that approximates bandgap approaching that of the 3D end-member at sufficiently high *n* values. Dion–Jacobson (DJ) quasi-2D HPs, which employ divalent diammonium spacers, are particularly appealing due to their shortened interlayer spacing and elimination of van der Waals gaps compared to Ruddlesden–Popper (RP) analogues,[18] resulting in structural rigidity and enhanced stability.[19–22] However, reproducibly directing phase evolution toward a stable 3D-like phase within quasi-2D films remains challenging, as nonequilibrium processing conditions and a vast, interdependent parameter space drive the concurrent formation of multiple crystallographic phases.[23] Even minor variations in precursor ratios, concentrations, or thermal conditions can significantly alter the final phase compositions, underscoring the limitations of traditional trial-and-error synthesis for systematic phase control. Moreover, the crystallization dynamics of DJ systems remain poorly understood relative to their RP counterparts. Although recent studies have begun to examine DJ phase formation using *in situ* structural probes,[24,25] real-time optical monitoring of DJ crystallization particularly PL-based tracking of phase evolution during thermal annealing, has not been established. This gap is consequential, because 3D-like, high-*n*, and low-*n* phases compete within a narrow crystallization window, no single diagnostic tool can reliably capture both the optical signatures of phase emergence and the structural identity of the resulting phases. Coupled optical and structural feedback is therefore essential for both mechanistic understanding and targeted phase selection. In addition, controlling the crystallization pathway toward a single target phase therefore requires both a mechanistic understanding of how spacer chemistry governs phase evolution and a systematic strategy for navigating the resulting compositional space.

Self-driving laboratories (SDLs) have emerged as a powerful approach for navigating the synthesis challenges inherent in HPs.[26–29] By combining automated high-throughput experimentation, rapid characterization, and machine learning (ML), SDLs enable systematic exploration of parameter spaces that governs phase formation and functional properties of HPs.[30–34] Robotic platforms allow precise control of reagent delivery, mixing, heating, and precursor composition[31,35] enabling reproducible control of nonequilibrium synthetic processes, an essential prerequisite for steering crystallization toward a target phase rather than a mixture of competing polymorphs. However, individual SDL platforms have typically relied on a single characterization modality, limiting their ability to cross validate optical and structural outcomes. Thus, reliable validated decision-making in SDLs requires integrating complementary characterization modalities within a unified cross facility framework.

In this work, we introduce a high-throughput, automated, ML-guided closed-loop workflow to systematically explore the compositional space of DJ quasi-2D HPs and achieve targeted 3D-like phase selection. Unlike conventional automated workflows that rely on a single feedback source, our approach uniquely integrates a cross-facility architecture in which experimental decisions are guided by data from complementary characterization modalities. As an initial step, we employ an automated *in situ* Photoluminescence (PL) module built on SPINBOT, a robotic spin-coating platform to directly probe crystallization kinetics of DJ quasi-2D HPs during thermal annealing, a process that had previously been inferred mostly from RP analogues.[36–38] We selected two structurally distinct DJ spacers: 1,4-butanediammonium (BDA), a short-chain linear cation that promotes strong binding to the inorganic framework,[39,40] and 3-(aminomethyl)piperidinium (3AMP), a cyclic aliphatic cation with a piperidine ring,[21,41] to investigate how spacer geometry and molecular rigidity influence crystallization kinetics and phase evolution in FA-based quasi-2D HPs. *In situ* PL observations revealed that combining these two co-spacers with $FAPbI_3$ enables tunable modulation of crystallization dynamics, allowing the overall crystallization rate to be adjusted to direct growth toward the 3D-like target phase. Guided by this, automated high-throughput synthesis was used to construct a ternary compositional library spanning the $FAPbI_3$, $BDAPbI_4$ and $3AMPPbI_4$ space, screening 480 compositions across five iterative rounds. This workflow advances existing SDL frameworks[28,42] by introducing a cross-facility feedback loop that couples optical and structural diagnostics, within a Gated Active Learning architecture developed by Liu.[43,44] High-throughput PL characterization provides rapid feedback on phase evolution and stability, while XRD similarity scoring serves as a structural filter to evaluate correspondence with the target 3D-like phase. Together, these complementary diagnostics, enables data-driven identification of compositions that satisfy both optical and crystallographic criteria. This workflow reveals two distinct compositional regimes, BDA-rich and 3AMP-rich, in which the kinetic balance between BDA-driven nucleation and 3AMP-mediated lattice relaxation converges on the target 3D-like phase, establishing co-spacer engineering as a design strategy for deterministic phase selection in DJ quasi-2D HPs.

© 2026 The Author(s). Published by the Royal Society of Chemistry

Automated experimentation workflow

Fig. 1 illustrates the automated workflow used for targeted 3D-like phase selection in quasi-2D HPs. In the first stage, automated *in situ* PL characterization provides insight into co-spacer-dependent crystallization kinetics and phase evolution during thermal annealing, and was used to identify the BDAPbI4 : 3AMPPbI$_4$ [BDA : 3AMP] co-spacer system as a suitable platform for 3D-like phase targeting in FA-based quasi-2D HPs (Fig. 1a). Guided by these observations, automated high-throughput synthesis was carried out using a pipetting robot to generate combinatorial film libraries spanning the ternary compositional space defined by FAPbI$_3$, BDAPbI$_4$, and 3AMPPbI$_4$, followed by automated PL characterization of the resulting films (Fig. 1b). In the initial iteration, a library of 96 films was synthesized, and the resulting PL data analyzed using a gated Gaussian process Beysian Optimization (GP–BO) framework. A primary GP model prioritized compositions exhibiting PL peak positions characteristic of the target 3D-like emission (~790 nm).[16,45] A secondary GP model evaluated a stability score derived from the time-dependent PL response, incorporating three spectral features including emission intensity, peak position, and full width at half maximum (FWHM). The stability score was defined as a weighted sum of normalized changes in emission intensity, peak position, and FWHM between initial and final measurements, with an additive penalty for compositions exhibiting multiple spectral peaks; lower values of stability score indicate greater temporal stability of the 3D-like emission. Although PL intensity was included in the stability score through its normalized temporal change, absolute PL intensity was not used as an independent optimization objective because it can be influenced by variations in film quality, defect properties, *etc.* across the high-throughput sample array. Therefore, the analysis emphasizes the relative temporal evolution of PL intensity within each sample rather than direct comparison of absolute intensities among different compositions. New compositions for each round were selected *via* an Upper Confidence Bound (UCB) acquisition function operating over both GP objectives (detailed implementation of the data analysis workflow, including pre-processing, stability-score calculation, GP modeling, and acquisition-function selection, is provided in the accompanying GitHub repository). Together these two objectives guided an acquisition function to select new compositions for subsequent synthesis, enabling iterative active learning over five rounds. Each library of 96 films required ~20 min to synthesize, and in total, 480 compositions were evaluated consuming only ~3 mL of precursor solution per batch, demonstrating the material efficiency and speed of the approach. Finally, XRD similarity scoring was performed on 12 candidate compositions selected on the basis of their PL signatures, providing structural validation and identification of the compositions with the closest crystallographic correspondence to the target 3D-like phase (Fig. 1c). By sequentially integrating kinetic insight, optical screening, and structural feedback within a single closed-loop framework, this workflow enables rapid, resource-efficient and data-driven convergence toward targeted quasi-2D compositions.

To investigate how spacer geometry and molecular rigidity influence phase evolution in FA-based DJ quasi-2D HPs, we selected two structurally distinct DJ spacers. 1,4-butanediammonium (BDA), a short-chain linear diammonium

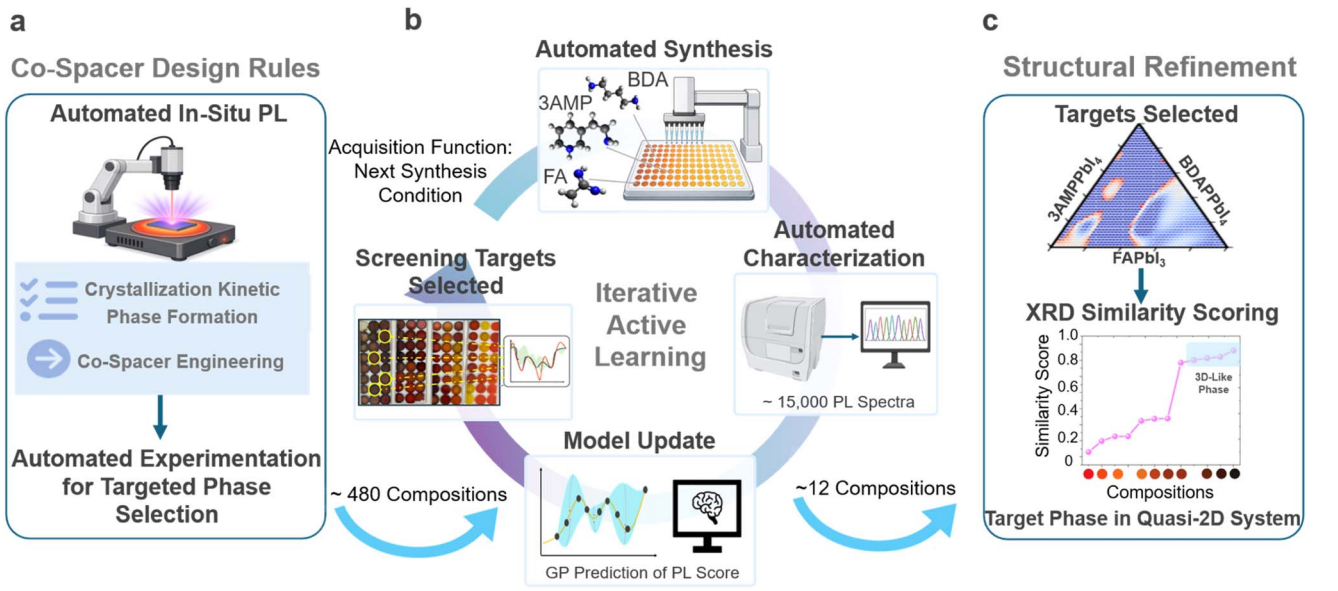

Fig. 1 Schematic of the automated workflow for targeted phase selection in quasi-2D HPs. (a) Automated *in situ* PL reveals co-spacer-dependent crystallization kinetics and phase-evolution behavior, (b) a pipetting-robot-based high-throughput synthesis workflow fabricates combinatorial film libraries across the ternary 3D : 2D compositional space, followed by automated PL characterization and GP–BO guided active learning for iterative composition selection. (c) XRD similarity scoring provides structural refinement to identify compositions that best match the target 3D-like phase. (Schematics of automated *in situ* PL and automated synthesis robot are made by AI).

© 2026 The Author(s). Published by the Royal Society of Chemistry

cation, and 3-(aminomethyl)piperidinium (3AMP), a cyclic aliphatic cation bearing a piperidine ring. Spacer geometry and molecular rigidity are known to influence the structural, electronic, and crystallization properties of DJ quasi-2D HPs, with compact linear spacers favoring stronger inorganic framework binding, while bulkier cyclic spacers impose greater steric constraints that modulate interlayer interactions.[46,47] These two spacers were therefore selected to represent contrasting structural extremes with the expectation that their distinct molecular geometries would differentially govern phase evolution trajectories during film formation. To directly probe these differences, automated *in situ* PL measurements were performed on spin-coated thin films during thermal annealing at 130 °C, yielding time-dependant PL spectra collected every second over a five-minute annealing period. Films were deposited inside an N_2-filled glovebox using a robotic spin-coating platform to ensure reproducible deposition under controlled atmospheric conditions, with PL emission continuously monitored from the moment the substrate was placed on the hotplate (Fig. 2a). As a first step, we examined binary FA systems, $FAPbI_3$: $BDAPbI_4$ and $FAPbI_3$: $3AMPPbI_4$, independently, to isolate the influence of each spacer on phase evolution before considering their combined effect.

Fig. 2b presents *in situ* PL spectra of $FAPbI_3$: $BDAPbI_4$ binary composition [%90 : %10] selected to assess how spacer concentration affects phase evolution in a 3D-dominant regime. In this composition, a relatively broad emission band centered near 800 nm appears immediately upon annealing and progressively narrows over time. This spectral narrowing is consistent with an evolution from a mixed population of emissive phases, likely including 3D-like phase and high-*n* quasi-2D domains,[15] toward a more spectrally uniform emission, suggesting progressive phase homogenization as annealing proceeds.[48] The immediate PL onset and rapid spectral narrowing suggest a relatively fast film crystallization, consistent with the short-chain linear geometry of BDA spacer, facilitating early framework formation.[36,49] However, the accompanying decrease in PL intensity over time is likely due to enhanced nonradiative recombination, which may reflect structural disorder arising from rapid crystallization, including non-uniform grain growth or introduction of defect states[50] that can compromise long-term phase stability and optoelectronic performance.[51]

In contrast, binary composition of $FAPbI_3$: $3AMPPbI_4$ [% 90 : %10], shown in Fig. 2c, exhibit a delayed PL onset, with emission emerging after 84 s of annealing, markedly later than immediate response observed in BDA-based films. This delayed appearance of emissive domains is consistent with slower film crystallization, likely associated with the bulkier cyclic structure of 3AMP spacer, whose steric hindrance may impede rapid framework formation.[46,52,53] Additionally, the resulting PL spectra is broader than those of BDA-based films, with the emission at lower wavelengths, suggesting the coexistence of multiple emissive phases, including lower-*n* quasi 2D domains alongside higher-*n* species. The broader spectral features and the persistence of lower-*n* emission are consistent with a slower phase evolution in which intermediate phases are not rapidly converted, in contrast to the behavior observed with BDA. While slower crystallization may in principle promote more uniform grain growth, it also prolongs the lifetime of intermediate low-*n* phases, presenting a challenging for achieving complete conversion into 3D-like phase under these annealing condition. *In situ* PL has been used in previous studies as an initial optical probe of phase evolution in quasi-2D perovskites, because the temporal emergence, shifting, and disappearance of emission features can provide insight into the evolution of different emissive domains during crystallization.[54–56] However, PL emission alone does not uniquely determine phase dimensionality or crystallographic identity. Therefore, the shorter- and longer-wavelength transient features observed here are interpreted as being spectrally consistent with possible lower-*n* and higher-*n* emissive domains, respectively, rather than as definitive structural identification of these transient phas.

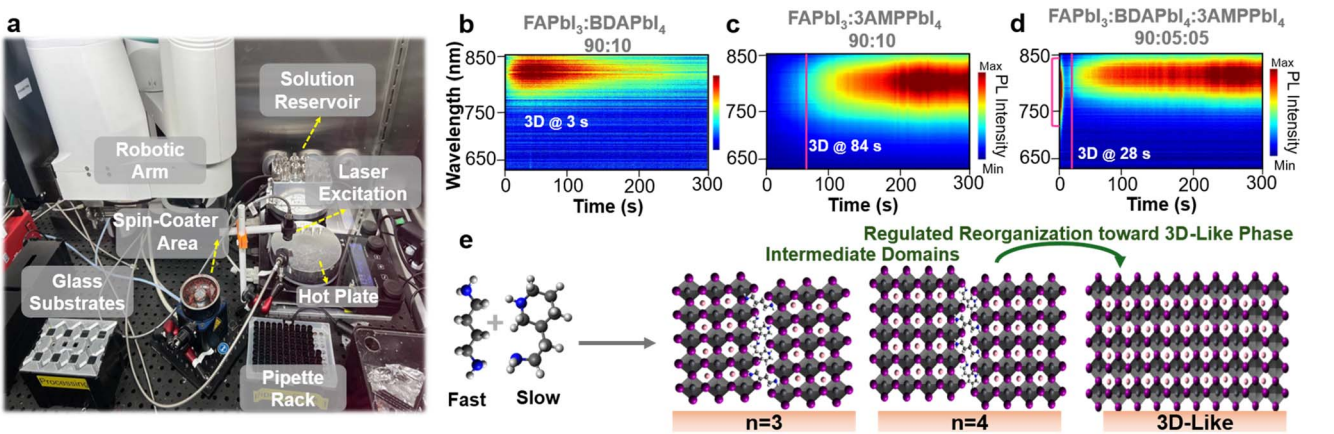

Fig. 2 (a) Photograph of the automated *in situ* PL setup built on the SPINBOT robotic platform, (b–d) 2D maps of *in situ* PL spectra collected every one second over a five-minute annealing period at 130 °C for selected compositions of quasi-2D films, (e) schematic illustration of the proposed co-spacer-dependent crystallization pathway based on *in situ* PL observations, showing how the BDA : 3AMP ratio modulates the formation of early intermediate domains and their subsequent evolution toward the target 3D-like phase.

© 2026 The Author(s). Published by the Royal Society of Chemistry

To explore whether combining the two spacers could redirect the crystallization pathway, we examined a ternary composition with low total spacer content, (10% total, FA : BDA : 3AMP = 90 : 05 : 05; Fig. 2d). In this composition, a broad initial PL band with a FWHM of ~120 nm (710–830 nm) appears immediately upon annealing and rapidly disappears within ~10 s, followed by the emergence of a stable emission near 790 nm after ~26 s. The early broad feature is spectrally distinct from both the BDA-based and 3AMP-based binary responses, suggesting the transient presence of emissive intermediate domains whose character is modulated by the co-spacer combination. While the precise structural identity of these early emissive species cannot be determined from PL alone, their rapid disappearance and the subsequent emergence of stable 3D-like emission are consistent with a scenario in which short-lived intermediate domains undergo structural reorganization to yield the 3D-like phase.[55] As illustrated in Fig. 2e, we propose a co-spacer-mediated crystallization pathway based on the *in situ* PL observations, in which the co-spacer ratio influences both the nature of early-forming intermediate domains and the rate at which they evolve toward the 3D-like phase. In this proposed model, co-spacer engineering modulates the early stages of the crystallization trajectory and direct phase evolution toward the target 3D-like structure. Taken together, the binary and ternary *in situ* PL data suggest that BDA and 3AMP play distinct and complementary roles in governing phase evolution, and that their combined use enables modulation of the crystallization pathway in ways not accessible with either spacer alone.

To examine how spacer chemistry influences film crystallinity, XRD measurements were performed on these compositions (Fig. S1). All three films exhibit diffraction peaks assigned to (001) and (002) reflections, consistent with quasi-2D HP structure, confirming the formation of mixed HP structures under these conditions.[16] Distinct differences in peak intensity and line shape reveal composition-dependant variations in crystallinity and preferred orientation. The 3AMP-based film displays the strongest and sharpest diffraction features, with particularly intense low-angle reflections, indicative of highly crystalline domains and a preferential vertical orientation of the perovskite layers,[16,57] though grazing-incidence measurements would be needed to confirm the out-of-plane texture unambiguously. The BDA-based film, by contrast shows weaker diffraction peaks accompanied by a diffuse background, likely due to structural disordered or partially amorphous regions[58] (Fig. S1b) an observation in agreement with its rapid PL onset. This suggest that fast crystallization of BDA limits complete lattice reorganization. The co-spacer film exhibits intermediate behavior, where the peak intensities are stronger and lineshapes are sharper than in the BDA-only film, and the diffuse background is absent, suggesting improved crystalline order relative to the BDA-only case. The combined analysis of *in situ* PL and XRD results indicate that incorporating both spacers with FA modulates the crystallization process in a way that partially mitigates the structural disorder associated with BDA-only rapid crystallization, while avoiding the prolonged lower-*n* phases persistence seen with 3AMP alone.

Automated high throughput synthesis and multimodal characterization platform

Building on the kinetic insights from *in situ* PL, an automated closed-loop workflow was employed to iteratively identify $FAPbI_3$: $BDAPbI_4$: $3AMPPbI_4$ compositional ratios capable of directing phase evolution toward the targeted 3D-like phase across the full ternary space. In each iteration, a combinatorial library of 96 unique printed films spanning the ternary compositional space was synthesized (Fig. S2a) using an automated pipetting platform and annealed at 130 °C for five minutes, yielding quasi-2D HP film arrays on glass substrate (Fig. S2b and c). Each library then subjected to high-throughput automated PL characterization, in which emission spectra were continuously collected over 10 h to capture the full temporal evolution of emission including any phase transitions occurring post-annealing under ambient-controlled conditions. These results used to update the gated GP–BO model for subsequent composition selection (Fig. S3). This iterative synthesis–characterization–learning cycle was repeated across five iterations, totalling 480 compositions evaluated. To visualize the initial phase landscape before model guided refinement, the resulting PL dataset was analyzed using Non-negative Matrix Factorization (NMF). NMF decomposes the complex time-dependent PL response into a set of characteristic spectral components and their composition-dependent weights, providing an unsupervised data-driven map of how the dominant emissive phases are distributed across the ternary space.[59] The number of NMF components was selected based on reconstruction error analysis, with three components found to adequately represent the dominant spectral features of the dataset. Fig. 3 shows the resulting NMF loading maps (top row) and the corresponding PL spectra in time domain (bottom row) for the first ternary library (Fig. S3), revealing distinct spatial distributions of emissive phases.

In BDA-rich compositions (Fig. 3a), the dominant NMF composnent is centered near ~790 nm with minimal spectral drift across the compositional space, consistent with the predominance of 3D-like emissive domains[48] and suppression of low-*n* phases. These observations qualitatively align with the *in situ* PL findings, suggesting that BDA-containing compositions favor rapid framework formation that kinetically promotes higher-*n* and 3D-like phase populations.[36] In contrast, 3AMP-rich compositions (Fig. 3b) are dominated by a shorter-wavelength PL component centered near 650 nm, consistent with the presence of lower-*n* quasi 2D phases,[60] in agreement with the delayed PL onset and broader spectral features observed in the 3AMP binary *in situ* PL data. The ternary co-spacer compositions (Fig. 3c) exhibit an NMF component spanning 720–800 nm, suggesting the coexistence of high-*n* quasi-2D and 3D-like phases, intermediate between the two binary extremes. Overall, the NMF analysis demonstrates that the dominant emissive phase population shifts systematically across the ternary space in a manner consistent with the crystallization behavior identified by *in situ* PL, confirming that

© 2026 The Author(s). Published by the Royal Society of Chemistry

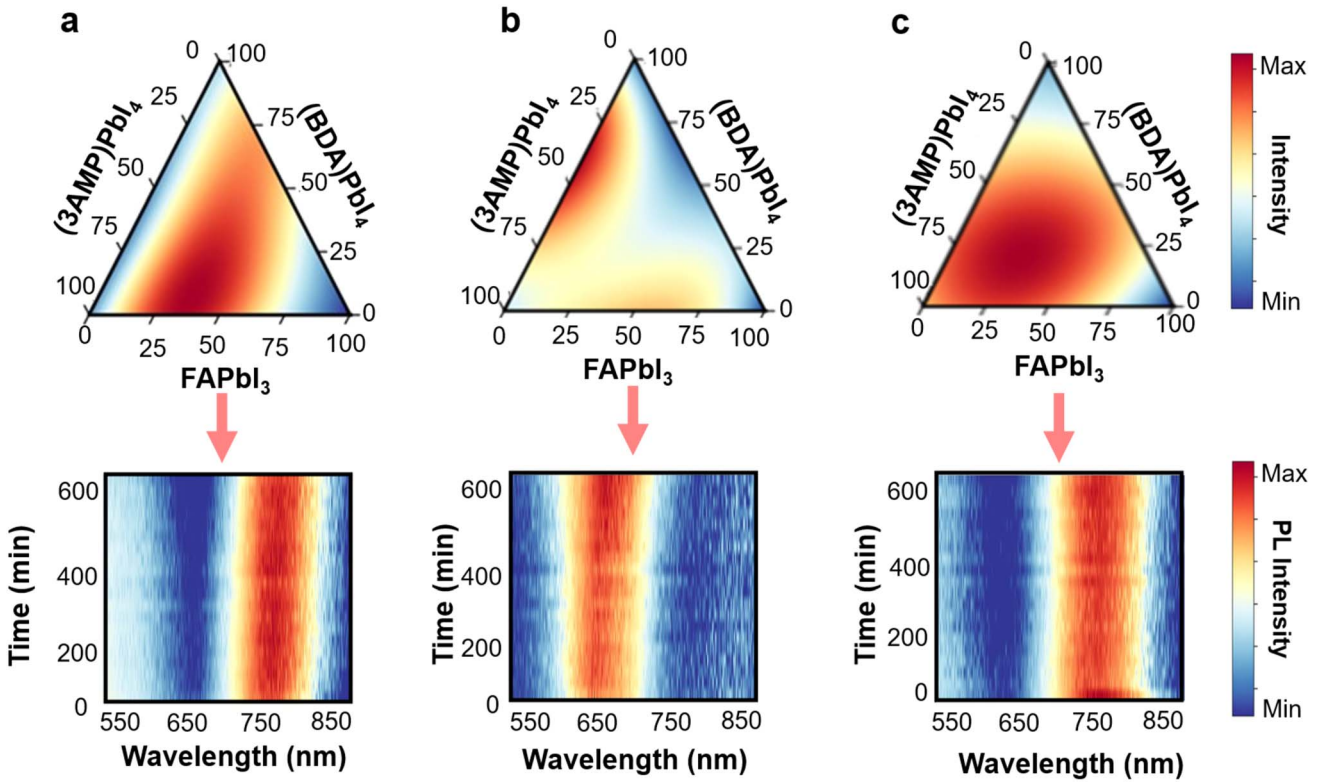

Fig. 3 (a–c) NMF-deconvoluted loading maps and PL components corresponding to the phases for the combinatorial libraries of quasi-2D HP films over 10 hours. The ternary diagrams are the compositional dependencies of the component intensities (top rows) and 2D NMF components (bottom rows) in each panel, describing the PL behavior of the corresponding phase diagram as a function of wavelength and time.

spacer-dependent phase evolution during annealing is reflected in the final film emission characteristics. Importantly, the co-spacer compositions occupy a distinct region of phase space, underscoring the potential of co-spacer engineering to expand the accessible quasi-2D phase landscape and enable targeted phase stabilization through compositional tuning.

Building on the phase landscape established from the initial combinatorial library, a gated GP–BO framework was employed to iteratively identify co-spacer compositions that favor stable 3D-like phase formation. The exploration was guided by two complementary optical objectives, a primary objective targeting PL peak positions characteristic of 3D-like emission (~790 nm), and a secondary stability score derived from the temporal evolution of PL spectral features over the 10 h measurement window. Compositions were selected at each iteration using an UCB acquisition function applied to the gated GP surrogate. Over five autonomous iterations, a total of 480 compositions were explored (Fig. S4). This closed-loop exploration progressively concentrated sampling toward region of ternary space that reproducibly produced stable 3D-like emission (Fig. 4a). In addition, a sensitivity analysis confirmed that reasonable variations in the weighting factors, wavelength tolerance, and multiphase penalty did not materially alter the composition ranking or the identified stable regions (Note S1 and Fig. S5). To evaluate the reliability of the GP–BO predictions, the posterior variance (uncertainty) and UCB acquisition surface, computed as the predicted stability score minus κ times the model uncertainty, reflecting the minimization objective, were mapped across the ternary compositional space (Fig. S6). The high effective-score region, enclosed by the green ellipse, aligns closely with the experimentally verified 3D-like compositional domain in Fig. 4a, indicating that the GP–BO framework effectively balanced exploration and exploitation to locate robust compositional optima. Moreover, the low predictive uncertainty in these regions confirms that the model converged with high confidence, providing a reliable basis for candidate selection in the subsequent structural refinement stage.

To establish a direct correspondence between optical stability and structural fidelity, XRD patterns of the top-performing compositions identified by gated GP–BO were quantitatively benchmarked against a reference 3D phase pattern using a similarity-scoring algorithm (Fig. 4b). XRD similarity scoring was performed by calculating the Structural Similarity Index Measure (SSIM) between each candidate diffraction pattern and a reference 3D phase pattern extracted from the ICSD computed over the full interpolated 2θ range following intensity normalization; higher SSIM values indicate closer crystallographic correspondence to the target 3D phase (detailed XRD similarity analysis and associated source code are provided in the accompanying GitHub repository). Two high-confidence compositional regions emerged from this analysis, one in the BDA-rich regime, where BDA content exceeds 3AMP, and a second in the 3AMP-rich regime, where 3AMP exceeds BDA.

© 2026 The Author(s). Published by the Royal Society of Chemistry

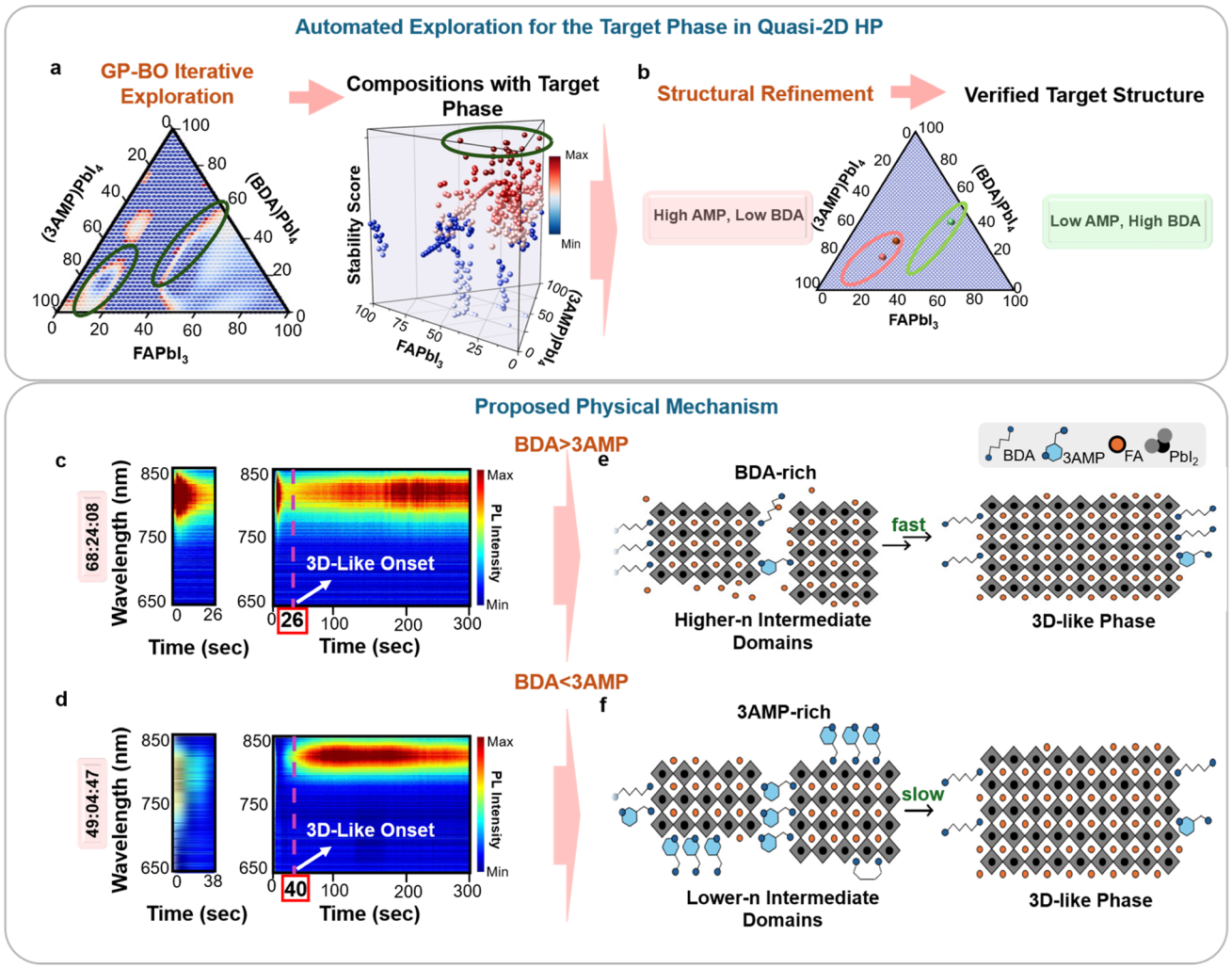

Fig. 4 (a) Final iteration of gated GP–BO exploration across the $FAPbI_3$: $BDAPbI_4$: $3AMPPbI_4$ ternary compositional space. The 3D compositional map represents the gated GP–BO stability score derived from temporal evolution of PL spectra. Red corresponds to compositions exhibiting stable target 3D-like PL emission, while blue indicates compositions lacking the target 3D-like phase. Green ellipses denote the high-confidence compositional regions selected for further structural validation. (b) Structural XRD refinement, the dots in the compositional map indicate 3D-like compositions. (c and d) *In situ* PL evolution during annealing at 130 °C (5 minutes) for (c) [FA : BDA : 3AMP] = [68 : 24 : 08], and (d) [49 : 04 : 47], showing 3D-like onset times of 26 s and 40 s, respectively. (e and f) Schematic illustration of the proposed crystallization pathways in BDA-rich *versus* 3AMP-rich compositions.

Two compositions with the highest similarity score was selected from the two regions for detailed validation, $FAPbI_3$: $BDAPbI_4$: $3AMPPbI_4$ = [68 : 24 : 08] and [49 : 04 : 47]. Films were deposited using the automated SPINBOT platform and their phase evolution monitored by *in situ* PL during annealing at 130 °C for 5 minutes (Fig. 4c and d). In both compositions, a broad initial emission band appears immediately upon heating and progressively diminishes, giving way to a stable, narrower emission near 790 nm that persist throughout the annealing period. The transient broad feature is spectrally distinct from the final 3D-like PL peak and is consistent with the presence of short-lived intermediate emissive domains formed during the earliest stages of crystallization, though their precise structural identity cannot be determined. Notably, the onset of 3D-like emission occurs at markedly different times, 26 s for compositions with [68 : 24 : 08] (Fig. 4c), and 40 s for [49 : 04 : 47] (Fig. 4d), indicating that the kinetics of 3D-like phase formation vary systematically with co-spacer ratios, in agreement with the distinct crystallization roles of BDA and 3AMP. Beyond differences in onset time, the spectral characteristics of the early transient emission also reveal composition-dependent phase evolution pathways. For the composition [68 : 24 : 08], the intermediate domains are centered at longer wavelengths (≈760–820 nm). By contrast, the 3AMP-rich composition [49 : 04 : 47] displays a broader emission of intermediate domains at ≈670–800 nm during the first 40 s of annealing (Fig. 4d), which is associated with slower phase evolution in which the developing Pb–I framework incorporates a more heterogeneous population of emissive domains before converging on the 3D-like phase. This is in line with the moderating role of 3AMP suggested by the binary *in situ* PL data in Fig. 2c. Importantly, in both compositions, these early emissive domains are transient.

© 2026 The Author(s). Published by the Royal Society of Chemistry

The broader and shorter-wavelength transient emission is consistent with the possible presence of lower-*n* quasi-2D domains, whereas the longer-wavelength features may reflect higher-*n* or 3D-like emissive populations. They diminish as the stable 3D-like emission near 790 nm emerges and persists, suggesting that regardless of the initial intermediate domains character, both co-spacer regimes can support convergence toward the target 3D-like phase under the identified compositional conditions (Fig. 4e and f). Thus, these observations suggest that stable 3D-like phase formation is favored when the BDA and 3AMP fractions are balanced such that framework formation proceeds rapidly enough to establish 3D-like connectivity, yet gradually enough to allow the emissive population to fully converge on the target phase.

The steady-state PL and XRD results of both compositions are shown in Fig. S7. Both films exhibit an emission near 790 nm and distinct XRD reflections corresponding to the 3D-like perovskite phase.[61,62] A weak peak near 12.6° is also observed, which can be attributed to residual/excess PbI_2 commonly seen in Pb-based HP films. Its low intensity indicates that PbI_2 is present only as a minor residual phase and does not dominate the overall structural response.[62,63]

To assess whether this convergence toward 3D-like emission reflects nanoscale spatially uniform phase formation and homogeneity, hyperspectral cathodoluminescence (CL) microscopy was performed on both validated compositions and shown in Fig. 5. For the BDA-rich composition [68 : 24 : 08], the SEM image (Fig. 5a, upper panel) shows large, laterally continous grains with smooth surfaces, consistent with a morphology resulting from relatively rapid grain growth and coalenscence during annealing. The corresponding 790 nm-filtered CL map (Fig. 5b, upper panel) is spatially uniform across the scanned region, indicating that the 3D-like phase is spatially distributed throughout the film rather than confined to isolated grains or local domains. Local CL spectra collected from six representative positions, including grain interiors, boundaries, and lower-intensity regions, all exhibit an emission centered near the 3D-like phase (Fig. 5c, upper panel). The absence of additional shorter-wavelength emission features suggests minimal contribution from lower-n phases or other emissive phase impurities within the mapped area. For the 3AMP rich composition FA : BDA : 3AMP [49 : 04 : 47], the SEM image in Fig. 5a (lower panel) shows smaller grains with partially faceted boundaries and noticeable intragrain contrast, indicating a slower and less complete grain-coarsening process under the same annealing conditions. The 790 nm-filtered CL intensity map (Fig. 5b, lower panel) exhibits modest spatial variations that mirroring this microstructural heterogeneity; however, six-point spectra collected from both bright and dim regions converge on a single band-edge emission, indicating that the emissive phase is spectrally consistent with the 3D-like structure across the mapped area despite the less uniform morphology. Importantly, the observation of spatially homogenous 3D-like emission in both compositions—despite their distinct grain morphologies and crystallization pathways—indicates that convergence toward the target emissive phase does not require a single specific microstructural outcome, but rather reflects the compositional balance between BDA and 3AMP that governs the phase evolution pathway. To compare the CL response of the workflow-selected compositions with that of compositions outside the identified phase-selection regions, we additionally performed CL measurements on

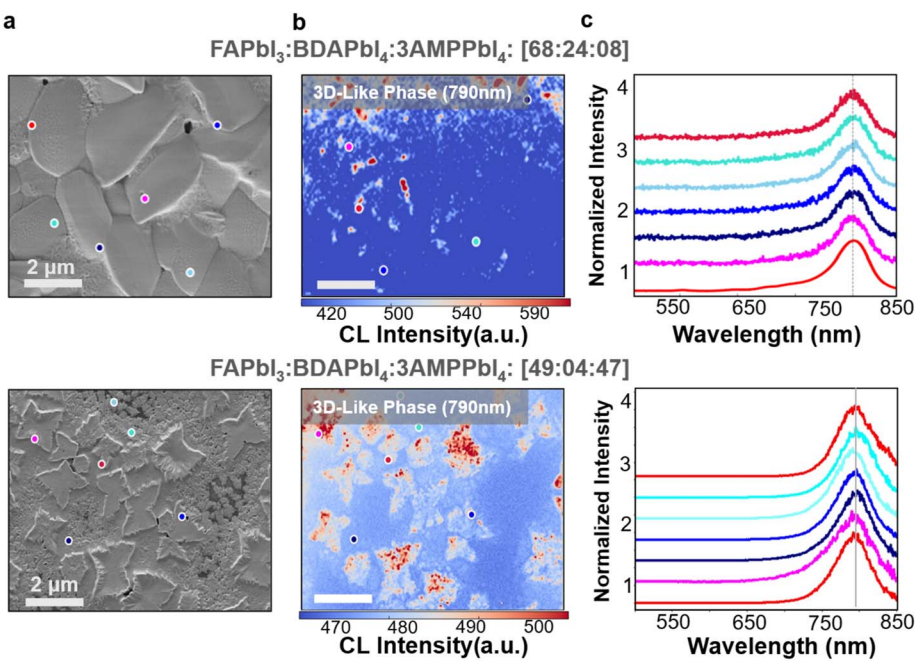

Fig. 5 Hyperspectral CL microscopy characterizations, (a) SEM images and the corresponding (b) 790 nm-filtered CL intensity maps corresponding to 3D-like phase of the DJ quasi-2D HP films with relative co-spacer ratios. (c) Local CL spectra collected at the six different spots (marked with colored circles in the SEM images and the CL maps) in each film.

© 2026 The Author(s). Published by the Royal Society of Chemistry

randomly selected co-spacer ratios in Fig. S8. For the BDA-rich films, SEM images reveal a relatively rough surface. Correspondingly, the CL maps show strong and spatially localized emission centered near the 3D-like phase emission. By contrast, the 3AMP-rich films exhibit smoother and more compact surfaces with flower-shaped grains. Their CL maps are dominated by shorter-wavelength emission associated with lower-*n* phases. The SEM image of composition containing both BDA and 3AMP reveal reduced surface roughness, while the CL maps also display emission near 790 nm with other n-phase contributions.

To access the practical relevance of our workflow-selected compositions, a preliminary photovoltaic (PV) device demonstration was performed using the DJ quasi-2D HP with a $FAPbI_3 : BDAPbI_4 : 3AMPPbI_4$ [68 : 24 : 08] composition. This composition was selected on the basis of its comparatively uniform CL emissive continous grain morphology. Motivated by this, *p–i–n* structured PV devices were fabricated using a standard architecture (details in Experimental section and Fig. S9). To benchmark this ternary composition against the corresponding binary systems, PV devices were also fabricated using [54 : 46 : 0] and [76 : 0 : 24] compositions under the same device architecture. As shown in Fig. S10a, the workflow-selected ternary composition exhibits the best device response among the three tested formulations, reaching a champion PCE of 15.39%, compared with lower performance from the two binary compositions, 11.27 and 8.62%, respectively. Average performance statistics across multiple devices are summarized in Table S1, and representative *J–V* characteristics are shown in Fig. S10b. The improved performance of the ternary composition is consistent with the optical results, where co-spacer tuning promotes formation of a more homogeneous 3D-like emissive phase compared with the binary systems. The EQE spectrum (Fig. S10c) is consistent with the optical bandgap expected for the 3D-like FA-based DJ perovskite composition. It is noted that device fabrication employed additional processing steps not present in the high-throughput screening workflow; the composition identified here therefore represents a promising starting point for further device-level optimization rather than a fully optimized photovoltaic formulation. While this efficiency is modest relative to state-of-the-art DJ quasi-2D HP solar cells,[64–66] the comparison with binary devices demonstrates that the workflow-selected ternary composition provides a more favorable starting composition for functional PV integration. This demonstraties the practical downstream relevance of the autonomous phase-selection workflow.

Conclusion

This work introduces a multimodal, closed-loop autonomous workflow for targeted 3D-like phase selection in DJ quasi-2D HPs. It addresses a key challenge in the field, the lack of real-time kinetic insight into DJ crystallization pathways and the absence of a cross-validated, multi-diagnostic framework for deterministic phase control. By directly probing phase evolution during thermal annealing using automated *in situ* PL, we revealed that BDA and 3AMP play distinct but complementary roles in governing the crystallization trajectory toward the 3D-like phase. BDA-containing compositions exhibit rapid emergence of 3D-like emissive domains, consistent with fast framework formation, whereas 3AMP-containing compositions display slower phase evolution with a broader intermediate emissive population, consistent with a more gradual reorganization process. These composition-dependent behaviors, observed directly for the first time in a DJ quasi-2D system, provided the mechanistic basis for co-spacer selection and informed the design of the ternary compositional search space.

Guided by these kinetic observations, a gated GP–BO framework screened 480 compositions across five autonomous iterations, integrating high-throughput PL characterization with XRD similarity scoring to jointly evaluate optical and structural correspondence with the target 3D-like phase. This cross-facility coupling of complementary diagnostics, a capability not available in single-modality SDL workflows, enabled the identification of two distinct compositional regimes that converge on the target phase through kinetically distinct but complementary pathways. In BDA-rich compositions, the emissive population rapidly acquires 3D-like character, with 3AMP moderating the process and reducing structural heterogeneity. In 3AMP-rich compositions, slower phase evolution provides additional time for lattice reorganization. Spatial phase homogeneity across both regimes was confirmed by hyperspectral CL mapping, which revealed 3D-like band-edge emission across grain interiors, boundaries, and lower-intensity regions in both workflow-selected compositions, despite their distinct grain morphologies.

Beyond the specific material system studied here, this work establishes a practical cross-domain framework that links macroscopic optical responses during film formation to structural phase identity in the final film, demonstrating that targeted phase selection in kinetically governed quasi-2D HPs can be achieved through the systematic integration of *in situ* optical monitoring, combinatorial automated synthesis and characterization, and ML-guided exploration. The approach exemplifies a new generation of SDLs capable of learning simultaneously across optical, structural, and kinetic domains, and is in principle extensible to other quasi-2D HP systems and co-spacer combinations where phase control remains a central challenge.

Experimental section

Materials

Butane-1,4-diammonium iodide ($BDAI_2$; Greatcell Solar Materials, 98%), lead(II) iodide (PbI_2; Fisher Scientific, 99.99% ultra-dry, metals basis), *N*,*N*-dimethylformamide (DMF; Sigma-Aldrich, 99.8% anhydrous), dimethylsulfoxide (DMSO; Sigma-Aldrich, ≥99.9% anhydrous) were purchased and used without further purification. 3-(Aminomethyl)piperidinium lead iodide ($3AMPPbI_4$) was synthesized and kindly provided by Dr Kanatzidis's group at Northwestern University in USA, Dr Choi's group (Hanyang University) and Dr Yang's group (Yonsei University) in Korea.

© 2026 The Author(s). Published by the Royal Society of Chemistry

In situ PL characterization

Thin films for *in situ* PL measurement were prepared using a SPINBOT robotic spin-coating platform inside an N_2-filled glovebox. Stoichiometric precursor solutions were dispensed onto cleaned glass substrates, and a one-step spin-coating protocol (4000 rpm, 45 s) was executed. Immediately after coating, the substrates were robotically transferred from the spin station to an integrated hotplate maintained at 130 °C for annealing. During this thermal treatment, *in situ* PL spectra were continuously recorded with an automated optical system mounted over the hotplate. The optical configuration consisted of a 405 nm laser diode for excitation, a plano-convex focusing lens, a 450 nm long-pass filter to remove scattered excitation light, and a fiber-coupled Ocean Optics QE Pro spectrometer (factory calibrated). The detection head was positioned directly above the hotplate to monitor emission throughout the annealing process. PL spectra were acquired every one second for five minutes, providing real-time insight into phase evolution under rigorously oxygen- and moisture-free conditions.

High-throughput robotic synthesis of quasi-2D HP films

Stoichiometric quantities of $XPbI_4$ and (0.3 M) (X = BDA, 3AMP) were dissolved in a mixture solvent, DMF : DMSO (9 : 1 ratio), within an N_2-filled glovebox and stirred for three hours at room temperature. Subsequently, these solutions were transferred to a pipetting robot system maintained under an N_2 atmosphere. 50 μL of precursor solutions, representing 96 different 3D : 2D composition ratios, were dispensed into each well of a microplate. This was achieved using an opentron OT-2 pipetting robot. For film depositions, the glass substrates were ultrasonically cleaned sequentially in deionized water, isopropanol, and acetone. After drying the substrates with nitrogen, they underwent a 40-minute ultraviolet ozone treatment. Immediately after the treatment, the substrates were transferred into a robot within an N_2 atmosphere and placed on a hotplate. The temperature of the hotplate was set to 130 °C. 0.5 μL of each precursor solution was then dispersed onto the substrates using an 8-channel pipetting robot, a process that took only five minutes. After depositing all 96 compositions onto the substrates, they were left on the hotplate and annealed at 130 °C for 5 minutes, resulting in the formation of round films. The high-throughput robotic system operates entirely within an N_2-filled enclosure, where both humidity and temperature are closely monitored and recorded for each experiment, before and during synthesis. For this specific experiment, the humidity was maintained at 0.5% RH at a temperature of 24 °C during synthesize.

Automated photoluminescence characterization

The drop-casted films were quickly transferred to the hybrid multi-mode optical reader (BioTek, Cytation 5), situated adjacent to the robotic system. PL spectra, with a 1 nm step resolution, were then collected from each well over time, using an excitation wavelength of 365 nm. A consistent 'read' cycle was employed to gather 96 spectra from each film at 10-minute intervals, repeated across 100 cycles to obtain time-evolved PL spectra. This setup ensured that all films remained uninterrupted within the reader for the entire duration, thereby maintaining consistent time conditions for PL measurement across all compositions.

Data processing, machine learning and co-optimization

The cross-facility optimization approach was established within the framework of Gated Active Learning.[43,44] In this strategy, on-the-fly experimentation is guided by a primary GP–BO. Concurrently, promising samples identified through online characterization (diagnosis-1) can be transferred to *ex situ* facilities for more detailed or compensating characterization (diagnosis-2). A surrogate model, such as a secondary GP or another predictive model, can then be employed to estimate the unmeasured outcomes of diagnosis-2. These predictions are incorporated into the decision-making process for subsequent synthesis steps. In this way, the decision-making process not only adheres to the optimization objectives of the primary GP–BO but also integrates the insights obtained from in-depth characterization.

Data analysis was performed using python. The scripts, jupyter notebooks, and associated data files (PL and XRD) used for the analysis are publicly available through the GitHub repository: (https://github.com/ElhamFoadian/Automated-Multimodal-Experimentation-for-Co-Spacer-engineering-for-Phase-selection-in-Quasi-2D-HP).

Other characterizations

X-ray Diffraction (XRD) pattern of the films was acquired by using a high-resolution X-ray diffractometer (Malvern Panalytical, Empyrean). Hyperspectral CL microscopy data were collected by using an environmental SEM instrument (FEI, Quattro) with a Delmic Sparc CL collection module. An e-beam with an acceleration voltage of 5 kV (beam current of 28 pA) with a dynamic acquisition time ranging 500–1000 ms was used for CL measurements. The pixel size was fixed to 500×500 nm^2. All measurements were conducted in a low vacuum environment of 0.27 Torr with H_2O vapor, which alleviated sample charging while minimizing electron-beam-induced damage.

PV fabrication and characterizations

For precursor preparation, the recrystallized $FAPbI_3$ powder was used, which was synthesized as follows: stoichiometric FAI and PbI_2 were dissolved in 2-methoxyethanol (2 ME; 0.6 M) and stirred until complete dissolution. This solution was filtered through a 0.45 μm PVDF membrane filter and heated in a round-bottom flask to ~120 °C. As the reaction progressed, a black precipitate gradually appeared, after which chlorobenzene was slowly added dropwise to promote crystallization. The precipitate was collected by filtration and washed with ether. The product was filtered, washed with diethyl ether, and dried for further use.

The p-i-n-type quasi-2D HP PVs were fabricated with the structure FTO/MeO-2PACz/quasi-2D HP/C_{60}/BCP/Ag. ITO-patterned glass substrates (1.5×1.5 cm^2) were sequentially

© 2026 The Author(s). Published by the Royal Society of Chemistry

cleaned by sonication in detergent, acetone, and isopropanol, followed by ultraviolet-ozone treatment for 20 min. MeO-2PACz as a hole-transporting molecule (0.5 mg mL^{-1} in ethanol) was spin-coated on the substrate at 3000 rpm for 30 s and subsequently annealed at 100 °C for 10 min. These substrates are then transferred into the N_2-filled glove box. 1 M of quasi-2D HP precursor solution was prepared by dissolving $FAPbI_3$ (68 mol%), $BDAPbI_4$ (24 mol%), and $3AMPPbI_4$ (8 mol%) in DMF : DMSO (9 : 1) solvent system, with 10 mol% of MACl as an additive to support crystallization. The quasi-2D HP films were deposited by spin-coating the solution onto the MeO-2PACz-coated substrates at 5000 rpm for 30 s. Note that the substrates were preheated at 80 °C and transferred to the vacuum chuck right before the spin-coating process. During spinning, 0.2 mL of hot chlorobenzene (CB), heated at 130 °C, was rapidly dropped in the final 10 s, followed by thermal annealing at 130 °C for 5 minutes. Electron transport layers and electrodes were deposited by thermal evaporation under $\sim 10^{-6}$ Torr. A 30 nm C_{60} layer was deposited at a rate of 0.2–0.4 Å s^{-1}, followed by 7 nm BCP at 0.1–0.2 Å s^{-1} and 120 nm Ag at 0.1–1 Å s^{-1}.

Photovoltaic performance of the devices was evaluated under simulated AM 1.5 G illumination (100 mW cm^{-2}) using an Oriel LCS-100 Series Small Area Solar Simulator. The measurement setup was housed in an N_2-filled glove box and connected to a Keithley 2400 SourceMeter for *J–V* characterization. A black shadow mask with an aperture of 0.0314 cm^2 was employed to define the active area and minimize photocurrent overestimation. External quantum efficiency (EQE) spectra were measured using a PV measurement QE system with monochromatic illumination provided by a Xenon lamp.

Conflicts of interest

There are no conflicts to declare.

Data availability

The data supporting this article are included in the supplementary information (SI) and Experimental section. The automated multimodal experimentation workflow and data analysis were implemented using python. Python scripts and notebooks, and associated data files are publicly available in the GitHub repository: https://github.com/ElhamFoadian/Automated-Multimodal-Experimentation-for-Co-Spacer-engineering-for-Phase-selection-in-Quasi-2D-HP. Supplementary information is available. See DOI: https://doi.org/10.1039/d6el00105j.

Acknowledgements

E. F., S. S. and M. A. acknowledge support from the National Science Foundation (NSF), award number 2043205. E. F. acknowledges partial support from the Center for Materials Processing (CMP) at the University of Tennessee, Knoxville. Work at Northwestern was supported in part by the National Science Foundation under Grant No. DMR-2019444 (NSF Center for Integration of Modern Optoelectronic Materials on Demand, IMOD). This cross-facility optimization workflow development (Y. L.) was sponsored by the INTERSECT Initiative as part of the Laboratory Directed Research and Development Program of Oak Ridge National Laboratory, managed by UT-Battelle, LLC for the US Department of Energy under contract DE-AC05-00OR22725. The CL experiments and workflow implementation (partially) were supported by the Center for Nanophase Materials Sciences (CNMS), which is a US Department of Energy, Office of Science User Facility at Oak Ridge National Laboratory.

References

1 H. Min, M. Kim, S.-U. Lee, H. Kim, G. Kim, K. Choi, J. H. Lee and S. I. Seok, Efficient, stable solar cells by using inherent bandgap of α-phase formamidinium lead iodide, *Science*, 2019, **366**(6466), 749–753.
2 F. F. Targhi, Y. S. Jalili and F. Kanjouri, MAPbI3 and FAPbI3 perovskites as solar cells: Case study on structural, electrical and optical properties, *Results Phys.*, 2018, **10**, 616–627.
3 G. Mannino, I. Deretzis, E. Smecca, A. La Magna, A. Alberti, D. Ceratti and D. Cahen, Temperature-dependent optical band gap in CsPbBr3, MAPbBr3, and FAPbBr3 single crystals, *J. Phys. Chem. Lett.*, 2020, **11**(7), 2490–2496.
4 J. Jeong, M. Kim, J. Seo, H. Lu, P. Ahlawat, A. Mishra, Y. Yang, M. A. Hope, F. T. Eickemeyer, M. Kim, *et al.*, Pseudo-halide anion engineering for alpha-FAPbI(3) perovskite solar cells, *Nature*, 2021, **592**(7854), 381–385, DOI: 10.1038/s41586-021-03406-5FromNLMPubMed-not-MEDLINE.
5 H. Lu, Y. Liu, P. Ahlawat, A. Mishra, W. R. Tress, F. T. Eickemeyer, Y. Yang, F. Fu, Z. Wang and C. E. Avalos, Vapor-assisted deposition of highly efficient, stable black-phase FAPbI3 perovskite solar cells, *Science*, 2020, **370**(6512), eabb8985.
6 L. M. Pazos-Outón, T. P. Xiao and E. Yablonovitch, Fundamental efficiency limit of lead iodide perovskite solar cells, *J. Phys. Chem. Lett.*, 2018, **9**(7), 1703–1711.
7 K. Wang, L. Zheng, Y. Hou, A. Nozariasbmarz, B. Poudel, J. Yoon, T. Ye, D. Yang, A. V. Pogrebnyakov and V. Gopalan, Overcoming Shockley-Queisser limit using halide perovskite platform?, *Joule*, 2022, **6**(4), 756–771.
8 A. Binek, F. C. Hanusch, P. Docampo and T. Bein, Stabilization of the trigonal high-temperature phase of formamidinium lead iodide, *J. Phys. Chem. Lett.*, 2015, **6**(7), 1249–1253.
9 O. Weber, B. Charles and M. Weller, Phase behaviour and composition in the formamidinium–methylammonium hybrid lead iodide perovskite solid solution, *J. Mater. Chem. A*, 2016, **4**(40), 15375–15382.
10 J. V. Milić, S. M. Zakeeruddin and M. Grätzel, Layered hybrid formamidinium lead iodide perovskites: challenges and opportunities, *Acc. Chem. Res.*, 2021, **54**(12), 2729–2740.
11 L. Wang, X. Wang, L.-L. Deng, S. Leng, X. Guo, C.-H. Tan, W. C. Choy and C.-C. Chen, The mechanism of universal green antisolvents for intermediate phase controlled high-efficiency formamidinium-based perovskite solar cells, *Mater. Horiz.*, 2020, **7**(3), 934–942.

© 2026 The Author(s). Published by the Royal Society of Chemistry

12 K. Wang, Z.-Y. Lin, Z. Zhang, L. Jin, K. Ma, A. H. Coffey, H. R. Atapattu, Y. Gao, J. Y. Park and Z. Wei, Suppressing phase disproportionation in quasi-2D perovskite light-emitting diodes, *Nat. Commun.*, 2023, **14**(1), 397.
13 S. Masi, A. F. Gualdron-Reyes and I. Mora-Sero, Stabilization of black perovskite phase in FAPbI3 and CsPbI3, *ACS Energy Lett.*, 2020, **5**(6), 1974–1985.
14 Z. Zheng, S. Wang, Y. Hu, Y. Rong, A. Mei and H. Han, Development of formamidinium lead iodide-based perovskite solar cells: efficiency and stability, *Chem. Sci.*, 2022, **13**(8), 2167–2183.
15 M. Um, S. L. Sanchez, H. Song, B. J. Lawrie, H. Ahn, S. V. Kalinin, Y. Liu, H. Choi, J. Yang and M. Ahmadi, Tailoring Molecular Space to Navigate Phase Complexity in Cs-Based Quasi-2D Perovskites *via* Gated-Gaussian-Driven High-Throughput Discovery, *Adv. Energy Mater.*, 2025, **15**(16), 2404655.
16 J. Yang, J. Hidalgo, D. Song, S. V. Kalinin, J. P. Correa-Baena and M. Ahmadi, Accelerating Materials Discovery by High-Throughput GIWAXS Characterization of Quasi-2D Formamidinium Metal Halide Perovskites, *Adv. Funct. Mater.*, 2024, **34**(49), 2409293.
17 J.-W. Lee, Z. Dai, T.-H. Han, C. Choi, S.-Y. Chang, S.-J. Lee, N. De Marco, H. Zhao, P. Sun and Y. Huang, 2D perovskite stabilized phase-pure formamidinium perovskite solar cells, *Nat. Commun.*, 2018, **9**(1), 3021.
18 D. Ghosh, D. Acharya, L. Pedesseau, C. Katan, J. Even, S. Tretiak and A. J. Neukirch, Charge carrier dynamics in two-dimensional hybrid perovskites: Dion–Jacobson *vs.* Ruddlesden–Popper phases, *J. Mater. Chem. A*, 2020, **8**(42), 22009–22022.
19 X. Li, W. Ke, B. Traoré, P. Guo, I. Hadar, M. Kepenekian, J. Even, C. Katan, C. C. Stoumpos and R. D. Schaller, Two-dimensional Dion–Jacobson hybrid lead iodide perovskites with aromatic diammonium cations, *J. Am. Chem. Soc.*, 2019, **141**(32), 12880–12890.
20 E. S. Vasileiadou, B. Wang, I. Spanopoulos, I. Hadar, A. Navrotsky and M. G. Kanatzidis, Insight on the stability of thick layers in 2D Ruddlesden–Popper and Dion–Jacobson lead iodide perovskites, *J. Am. Chem. Soc.*, 2021, **143**(6), 2523–2536.
21 L. Mao, W. Ke, L. Pedesseau, Y. Wu, C. Katan, J. Even, M. R. Wasielewski, C. C. Stoumpos and M. G. Kanatzidis, Hybrid Dion–Jacobson 2D lead iodide perovskites, *J. Am. Chem. Soc.*, 2018, **140**(10), 3775–3783.
22 P. Huang, S. Kazim, M. Wang and S. Ahmad, Toward phase stability: Dion–Jacobson layered perovskite for solar cells, *ACS Energy Lett.*, 2019, **4**(12), 2960–2974.
23 H. Gu, J. Xia, C. Liang, Y. Chen, W. Huang and G. Xing, Phase-pure two-dimensional layered perovskite thin films, *Nat. Rev. Mater.*, 2023, **8**(8), 533–551.
24 S. Ramakrishnan, D. Song, Y. Xu, X. Zhang, G. Aksoy, M. Cotlet, M. Li, Y. Zhang and Q. Yu, Solvent-mediated formation of quasi-2D Dion-Jacobson phases on 3D perovskites for inverted solar cells over 23% efficiency, *Adv. Energy Mater.*, 2023, **13**(45), 2302240.
25 K. Sun, R. Guo, S. Liu, D. Guo, X. Jiang, L. F. Huber, Y. Liang, M. A. Reus, Z. Li and T. Guan, Deciphering structure and charge carrier behavior in reduced-dimensional perovskites, *Adv. Funct. Mater.*, 2024, **34**(52), 2411153.
26 S. Sadeghi, K. Mattsson, J. Glasheen, V. Lee, C. Stark, P. Jha, N. Mukhin, J. Li, A. Ghorai and N. Orouji, A self-driving fluidic lab for data-driven synthesis of lead-free perovskite nanocrystals, *Digital Discovery*, 2025, **4**(7), 1722–1733.
27 J. Zhang, J. Wu, O. Stroyuk, O. Raievska, L. Lüer, J. A. Hauch and C. J. Brabec, Self-driving AMADAP laboratory: Accelerating the discovery and optimization of emerging perovskite photovoltaics, *MRS Bull.*, 2024, **49**(12), 1284–1294.
28 B. P. MacLeod, F. G. Parlane, T. D. Morrissey, F. Häse, L. M. Roch, K. E. Dettelbach, R. Moreira, L. P. Yunker, M. B. Rooney and J. R. Deeth, Self-driving laboratory for accelerated discovery of thin-film materials, *Sci. Adv.*, 2020, **6**(20), eaaz8867.
29 H. Hysmith, E. Foadian, S. P. Padhy, S. V. Kalinin, R. G. Moore, O. S. Ovchinnikova and M. Ahmadi, The future of self-driving laboratories: from human in the loop interactive AI to gamification, *Digital Discovery*, 2024, **3**(4), 621–636.
30 S. Sadeghi, F. Bateni, T. Kim, D. Y. Son, J. A. Bennett, N. Orouji, V. S. Punati, C. Stark, T. D. Cerra and R. Awad, Autonomous nanomanufacturing of lead-free metal halide perovskite nanocrystals using a self-driving fluidic lab, *Nanoscale*, 2024, **16**(2), 580–591.
31 M. Abolhasani and E. Kumacheva, The rise of self-driving labs in chemical and materials sciences, *Nat. Synth.*, 2023, **2**(6), 483–492.
32 E. Foadian, S. L. Sanchez, S. B. Harris, B. J. Lawrie, A. Dubey, Y. Tang, B. Hu, J. Yang and M. Ahmadi, Impact of Halogen Groups on the Properties of PEA-Based 2D Pb–Sn Halide Perovskites, *Adv. Opt. Mater.*, 2025, **13**(11), 2403120.
33 E. Foadian, J. Yang, S. B. Harris, Y. Tang, C. M. Rouleau, S. Joy, K. R. Graham, B. J. Lawrie, B. Hu and M. Ahmadi, Decoding the Broadband Emission of 2D Pb-Sn Halide Perovskites through High-Throughput Exploration, *Adv. Funct. Mater.*, 2024, **34**(52), 2411164.
34 E. Foadian, S. Sanchez, J. Marshall, and M. Ahmadi Accelerating halide perovskite discovery *via* high-throughput synthesis and automated closed-loop experimentation. in *Organic, Hybrid, and Perovskite Photovoltaics XXVI*, SPIE, 2025, vol. 13589, pp. 36–41.
35 S. E. Lohse, J. R. Eller, S. T. Sivapalan, M. R. Plews and C. J. Murphy, A simple millifluidic benchtop reactor system for the high-throughput synthesis and functionalization of gold nanoparticles with different sizes and shapes, *ACS Nano*, 2013, **7**(5), 4135–4150.
36 Y. Xu, M. Wang, Y. Lei, Z. Ci and Z. Jin, Crystallization kinetics in 2D perovskite solar cells, *Adv. Energy Mater.*, 2020, **10**(43), 2002558.
37 N. Zhou, Y. Shen, L. Li, S. Tan, N. Liu, G. Zheng, Q. Chen and H. Zhou, Exploration of crystallization kinetics in quasi two-dimensional perovskite and high performance solar cells, *J. Am. Chem. Soc.*, 2018, **140**(1), 459–465.

© 2026 The Author(s). Published by the Royal Society of Chemistry

38 Y. Chen, J. Hu, Z. Xu, Z. Jiang, S. Chen, B. Xu, X. Xiao, X. Liu, K. Forberich and C. J. Brabec, Managing phase orientation and crystallinity of printed Dion–Jacobson 2D perovskite layers *via* controlling crystallization kinetics, *Adv. Funct. Mater.*, 2022, **32**(19), 2112146.

39 S. Gohri, J. Madan, D. Samajdar, S. Bhattarai, M. K. Mohammed, M. K. Hossain, M. F. Rahman, A. K. Al-Mousoi, E. A. Al-Ammar and R. Pandey, Achieving 24.6% efficiency in 2D perovskite solar cells: Bandgap tuning and MXene contact optimization in (BDA)(MA) n− 1PbnI3n+ 1 structures, *Chem. Phys. Lett.*, 2024, **845**, 141291.

40 T. Niu, H. Ren, B. Wu, Y. Xia, X. Xie, Y. Yang, X. Gao, Y. Chen and W. Huang, Reduced-dimensional perovskite enabled by organic diamine for efficient photovoltaics, *J. Phys. Chem. Lett.*, 2019, **10**(10), 2349–2356.

41 W. Ke, L. Mao, C. C. Stoumpos, J. Hoffman, I. Spanopoulos, A. D. Mohite and M. G. Kanatzidis, Compositional and solvent engineering in Dion–Jacobson 2D perovskites boosts solar cell efficiency and stability, *Adv. Energy Mater.*, 2019, **9**(10), 1803384.

42 A. A. Volk, R. W. Epps, D. T. Yonemoto, B. S. Masters, F. N. Castellano, K. G. Reyes and M. Abolhasani, AlphaFlow: autonomous discovery and optimization of multi-step chemistry using a self-driven fluidic lab guided by reinforcement learning, *Nat. Commun.*, 2023, **14**(1), 1403.

43 S. B. Harris, R. Vasudevan and Y. Liu, Active oversight and quality control in standard Bayesian optimization for autonomous experiments, *npj Comput. Mater.*, 2025, **11**(1), 23.

44 U. Pratiush, H. Funakubo, R. Vasudevan, S. V. Kalinin and Y. Liu, Scientific exploration with expert knowledge (SEEK) in autonomous scanning probe microscopy with active learning, *Digital Discovery*, 2025, **4**(1), 252–263.

45 H. Gu, A. Zhu, J. Xia, W. Li, J. Zheng, T. Yang, S. Li, N. Zhang, S. Mei and Y. Cai, Nanoscale phase management of the 2D/3D heterostructure toward efficient perovskite solar cells, *Sci. Bull.*, 2024, **69**(18), 2853–2861.

46 X. Li, J. M. Hoffman and M. G. Kanatzidis, The 2D halide perovskite rulebook: how the spacer influences everything from the structure to optoelectronic device efficiency, *Chem. Rev.*, 2021, **121**(4), 2230–2291.

47 Y. Liu, H. Zhou, Y. Ni, J. Guo, R. Lu, C. Li and X. Guo, Revealing stability origin of Dion-Jacobson 2D perovskites with different-rigidity organic cations, *Joule*, 2023, **7**(5), 1016–1032.

48 F. Ma, J. Li, W. Li, N. Lin, L. Wang and J. Qiao, Stable α/δ phase junction of formamidinium lead iodide perovskites for enhanced near-infrared emission, *Chem. Sci.*, 2017, **8**(1), 800–805.

49 Y. Zhang, Y. Liu, Z. Xu, Z. Yang and S. Liu, 2D Perovskite Single Crystals with Suppressed Ion Migration for High-Performance Planar-Type Photodetectors, *Small*, 2020, **16**(42), 2003145.

50 S. Wang, T. Yang, Y. Yang, Y. Du, W. Huang, L. Cheng, H. Li, P. Wang, Y. Wang and Y. Zhang, *In Situ* Self-Elimination of Defects *via* Controlled Perovskite Crystallization Dynamics for High-Performance Solar Cells, *Adv. Mater.*, 2023, **35**(42), 2305314.

51 C. Zhang, H. Li, C. Gong, Q. Zhuang, J. Chen and Z. Zang, Crystallization manipulation and holistic defect passivation toward stable and efficient inverted perovskite solar cells, *Energy Environ. Sci.*, 2023, **16**(9), 3825–3836.

52 Y. Miao, Y. Chen, H. Chen, X. Wang and Y. Zhao, Using steric hindrance to manipulate and stabilize metal halide perovskites for optoelectronics, *Chem. Sci.*, 2021, **12**(21), 7231–7247.

53 C. Xu, Z. Zhang, S. Zhang, H. Si, S. Ma, W. Fan, Z. Xiong, Q. Liao, A. Sattar and Z. Kang, Manipulation of perovskite crystallization kinetics *via* Lewis base additives, *Adv. Funct. Mater.*, 2021, **31**(13), 2009425.

54 A. Halder, M. B. Alghalayini, S. Cheng, N. Thalanki, T. M. Nguyen, A. R. Hering, D. K. Lee, S. Arnold, M. S. Leite and E. Barnard, AI-Driven Robot Enables Synthesis-Property Relation Prediction for Metal Halide Perovskites in Humid Atmosphere, *Adv. Energy Mater.*, 2025, **15**(34), 2502294.

55 K. Darabi, M. Chauhan, B. Guo, J. Wang, D. Seyitliyev, F. Bateni, T. Wang, M. Ghasemi, L. Taussig and N. Woodward, Cationic ligation guides quantum-well formation in layered hybrid perovskites, *Matter*, 2024, **7**(12), 4410–4425.

56 J. Hou, W. Li, H. Zhang, S. Sidhik, J. Fletcher, I. Metcalf, S. B. Anantharaman, X. Shuai, A. Mishra and J.-C. Blancon, Synthesis of 2D perovskite crystals *via* progressive transformation of quantum well thickness, *Nat. Synth.*, 2024, **3**(2), 265–275.

57 A. Zanetta, V. Larini, Vikram, F. Toniolo, B. Vishal, K. A. Elmestekawy, J. Du, A. Scardina, F. Faini and G. Pica, Vertically oriented low-dimensional perovskites for high-efficiency wide band gap perovskite solar cells, *Nat. Commun.*, 2024, **15**(1), 9069.

58 Y. Wang, X. Lü, W. Yang, T. Wen, L. Yang, X. Ren, L. Wang, Z. Lin and Y. Zhao, Pressure-induced phase transformation, reversible amorphization, and anomalous visible light response in organolead bromide perovskite, *J. Am. Chem. Soc.*, 2015, **137**(34), 11144–11149.

59 D. Lee and H. S. Seung, Algorithms for non-negative matrix factorization, *Adv. Neural Inf. Process. Syst.*, 2000, **13**, 556–562.

60 H. Li, S. Hu, H. Wang, X. Zhang, Y. Tong, H. Qi, P. Guo, G. Zhao, J. Gao and P. Liu, Control of n-phase distribution in quasi two-dimensional perovskite for efficient blue light-emitting diodes, *ACS Appl. Mater. Interfaces*, 2023, **15**(7), 9574–9583.

61 J. Yang, B. J. Lawrie, S. V. Kalinin and M. Ahmadi, High-Throughput Automated Exploration of Phase Growth Behaviors in Quasi-2D Formamidinium Metal Halide Perovskites, *Adv. Energy Mater.*, 2023, **13**(43), 2302337.

62 A. Jana, Q. Ba, A. S. Nissimagoudar and K. S. Kim, Formation of a photoactive quasi-2D formamidinium lead iodide perovskite in water, *J. Mater. Chem. A*, 2019, **7**(45), 25785–25790.

© 2026 The Author(s). Published by the Royal Society of Chemistry

63 H. Song, H.-B. Kim, S. C. Cho, J. Lee, J. Yang, W. H. Jeong, J. Y. Won, H. I. Jeong, J. Yeop and J. Y. Kim, Supramolecular design principles in pseudohalides for high-performance perovskite solar mini modules, *Joule*, 2024, **8**(8), 2283–2303.
64 I. Metcalf, S. Sidhik, H. Zhang, A. Agrawal, J. Persaud, J. Hou, J. Even and A. D. Mohite, Synergy of 3D and 2D perovskites for durable, efficient solar cells and beyond, *Chem. Rev.*, 2023, **123**(15), 9565–9652.
65 S. Sidhik, I. Metcalf, W. Li, T. Kodalle, C. J. Dolan, M. Khalili, J. Hou, F. Mandani, A. Torma and H. Zhang, Two-dimensional perovskite templates for durable, efficient formamidinium perovskite solar cells, *Science*, 2024, **384**(6701), 1227–1235.
66 C. Pramanik, R. Garai, N. P. Jasti, N. Nandi, A. D. Mohite and K. Narayan, Direct evaluation of perovskite solar cell performance and stability using transient and steady-state transport measurements, *Adv. Energy Mater.*, 2025, **15**(34), 2502346.

© 2026 The Author(s). Published by the Royal Society of Chemistry